Quantitative modelling of motion, temperature gyrations, and growth of inclusions in weld pool

T. Hong, W. Pitscheneder, and T. DebRoy

The velocity and temperature fields, the shape and size of the fusion zone, and the motion of the inclusions were calculated by the solution of equations of conservation of mass, momentum, and energy in three dimensions for various welding conditions. The loci and the temperature gyrations experienced by a large number of inclusions were calculated numerically to seek a statistically meaningful residence time distribution of the inclusions and the number of intensities of the temperature cycles experienced by these particles. Finally, both the growth and dissolution of the inclusions were considered to calculate their size distribution. The inclusions experienced considerable recirculatory motion and strong temperature gyrations along their paths in the weld pool. The temperature–time plots for most of the inclusion particles displayed several temperature peaks. However, about one-third of the particles experienced continuous cooling behaviour. The average number of the temperature peaks in the time–temperature plots and the average residence time of inclusions in the weld pool changed significantly with welding conditions. The calculated temperature–time–transformation diagrams of the inclusions showed that the temperature gyrations affected the growth rates and the size distributions of the inclusions. Good agreement between the calculated and measured inclusion size distributions indicates that important aspects of weld metal structure can be understood from the fundamentals of transport phenomena and kinetics.

Mr Hong and Professor DebRoy are in the Department of Materials Science and Engineering, Penn State University, 212 Steidle Building, University Park, PA 16802, USA and Mr Pitscheneder is in the Department of Physical Metallurgy and Materials Testing, University of Leoben, Leoben, Austria. *Manuscript received 15 June 1997.*

INTRODUCTION

Safety and reliability of welded joints depend on the geometry, composition, and structure of the weldments. In recent years efforts have been made[1,2] to understand quantitatively each of these factors, particularly weldment structure.[3–7] Since the relationship between structure and properties has been most thoroughly studied for crystalline materials, especially for metals and alloys, the desirable weld metal structure can readily be identified for most common engineering alloys. Therefore, an important goal of contemporary welding research is to identify the welding variable required to produce desirable weld metal and heat affected zone structures.

An important component of calculations of microstructure is knowledge of how the temperature varies with time in all locations of interest[8] within a weldment. The temperature histories are then used in an appropriate phase transformation model.[3,4] By comparing model predictions with independent experimental data, the calculation procedure can be validated and then used with a reasonable degree of confidence. The most important feature of this approach is its usefulness in quantitatively predicting trends in microstructure resulting from variations in both welding variables and weld metal composition.

Critical to the weld metal properties are the nature, amount, and distribution of various phases and the composition, morphology, and distribution of inclusions.[9–11] In low alloy steels, the existence of certain kinds of inclusions can improve toughness by promoting the formation of acicular ferrite, a high toughness ferrite phase. However, controlling the amount of inclusions in the structure is a critical task, since the presence of a large volume fraction of inclusions leads to poor properties. Oxide inclusions are the most common in steel weldments, although nitride and sulphide inclusions may also be present. The oxide inclusions in steel welds form by reactions between the dissolved deoxidising elements, such as aluminium, titanium, silicon, and manganese, and dissolved oxygen. The composition of the weld metal plays an important role in determining the chemical composition of the inclusions. Welding variables such as the voltage, current, and welding speed significantly influence the composition of various phases in the microstructure and the number density, size distribution, and composition of the inclusions. Therefore, it is desirable to predict the effect of welding variables on the inclusion characteristics.

In most previous studies, the stability and formation of inclusions in steels have been examined mainly from thermodynamic considerations. Only in recent years has work started on the kinetics of inclusion growth. Chai and Eagar[12,13] developed a relationship between the basicity of the slag and the oxygen concentration of the weld metal by considering slag–metal reactions. Their work showed that the primary reactions of importance are those involving silicon, manganese, and oxygen. Mitra and Eagar[14–16] were successful in predicting weld metal chemistry from knowledge of baseplate, wire, and flux compositions; they also pointed out[14] the difficulty of determining the weld metal oxygen concentration from welding variables. Grong *et al.*[11] developed a model to predict the deposit chemistry from slag–metal reactions. Kluken and Grong[9] proposed a model to predict inclusion characteristics such as volume fraction, size, and chemical composition from weld metal composition and welding conditions. They proposed that the inclusions form in the hot region of the weld pool and grow by Ostwald ripening in the cold region. An empirical formula to estimate the volume fraction of inclusions by considering the concentrations of oxygen and sulphur in the steel was developed. Bhadeshia and Svensson[4] predicted inclusion composition by considering sequential deoxidation. The deoxidation reactions during solidification are

affected by compositional changes. Olson *et al.*[17] suggested that the free energies of formation of various oxides are affected by solute enrichment.

Recently, Babu *et al.*[18,19] proposed a series of generally applicable temperature–time–transformation (TTT) diagrams for inclusion growth by considering the nucleation rates of inclusions and their subsequent growth. This recent work provides a quantitative method to estimate the effects of time and temperature on the composition and growth rate of inclusions for a given alloy composition. While such a model is useful for a general understanding of inclusion growth, the model can not relate welding conditions with inclusion characteristics. Indeed, it is the specifics of the temperature–time histories experienced by the inclusions that affect their composition and size distribution. Knowledge of temperature–time histories during the growth of a large number of individual inclusions is a prerequisite for the phenomenological understanding of the composition and size distribution of inclusions in the weld pool for a given set of welding conditions.

Inside the weld pool, molten liquid undergoes vigorous circulation[20,21] resulting from buoyancy, surface tension, and (when electric current is used) electromagnetic forces. Since the fluid flow in the weld pool is recirculatory in nature, an inclusion grows or dissolves while in a state of varying motion, experiencing thermal excursions within the weld pool during its entire life cycle. At any given instant, its velocity and temperature depend on the velocity and temperature fields prevailing in the weld pool. While the nucleation of inclusions can occur in various regions of the weld pool, the welding variables and the material of the workpiece determine the size and shape of the weld pool and the temperature and velocity fields. Calculation of transient velocity and temperature fields in a moving weld pool with a fair degree of accuracy is computationally intensive.[20] However, considerable advances have recently been made in the calculation of fluid flow and heat transfer in the weld pool and these calculations can provide significant insight into the welding process that can not be achieved otherwise. However, very little effort has been made to combine these powerful new capabilities to understand fusion zone microstructures and inclusion growth.

Meaningful tracking of the temperature and velocities of thousands of inclusion particles as they move through regions of varying temperatures is an arduous task even with the help of fast workstations. Motivation for undertaking such calculations arises from the fact that the growth rates of individual inclusion particles are determined by their temperature excursions and residence times at various temperatures. In order to understand the effects of welding variables and weld metal composition on the size distribution and the composition of inclusions from fundamentals, temperature histories and the residence times of a large number of growing inclusions must be understood for each welding condition. The present work seeks to understand inclusion growth in a low alloy steel weld pool by considering the path, temperature history, velocities, and oxygen diffusion kinetics during shield gas arc welding processes.

Table 1 Welding parameters selected to calculate particle tracking

	Arc voltage, V	Arc current, A	Welding velocity, mm s^{-1}
Case 1	27	200	12·7
Case 2	27	300	12·7
Case 3	27	500	12·7
Case 4	27	300	5·2
Case 5	27	300	23·2

CALCULATION

Numerical prediction of temperature and velocity fields in weld pool

The velocity and temperature fields, the shape and size of the fusion zone, and the motion of the inclusions are calculated from the solution of equations of conservation of mass, momentum, and energy in three dimensions for various values of welding variables. The governing equations are modified by formulating them in the coordinate system attached to the heat source. The net velocity in the computational domain is subdivided into the convective velocity of the liquid metal relative to the solid part of the workpiece and the welding velocity. The convective velocity of the fluid is treated as the primary unknown velocity. Therefore, the enthalpy–porosity technique[22,23] can easily be implemented for flow modelling in the mushy zone. The welding velocity also contributes to physically meaningful source terms in the momentum and energy equations that can be conveniently discretised using the upwind scheme.[24] A control volume technique, described by Patankar,[24,25] has been implemented for the discretisation of the governing equations. The SIMPLER algorithm[25] was used for the solution of the equations.

The technique used to account for the phase change is based on the works of Voller and Prakash[22] and Brent *et al.*[23] The total enthalpy of the material is represented as a sum of sensible heat and latent heat content. Liquid fraction and latent heat content are assumed to be a linear function of temperature. The modified energy equation is therefore given by

$$\nabla \cdot \rho \boldsymbol{V} h = \nabla \cdot (\kappa / C_p) \nabla h + S_l - \nabla \cdot \rho \boldsymbol{U} h \quad . \quad . \quad . \quad . \quad . \quad (1)$$

where ρ is the density, $\boldsymbol{V}$ is the convective component of the velocity, h is the sensible heat, κ is the thermal conductivity, C_p is the specific heat, S_l is the source term that accounts for latent heat of melting and convective transport of latent heat in the two phase region, and $\boldsymbol{U}$ is the welding velocity.

The model was verified by comparing experimental measurements of weld pool geometry and transient temperatures at several selected locations in the weldment with the corresponding results obtained from the model at different welding speeds for the shielded metal arc welding of mild steels.[26] Good agreement between the experimental and the predicted values of the weld pool width and depth and the transient temperature values was achieved.

Because of the symmetry of the workpiece, the computational domain was limited to half of the plate to save computational effort. A $50 \times 28 \times 26$ non-uniform computational mesh was used to obtain maximum resolution. The grids were finer near the heat source in all three directions. Welding parameters and the data used for the calculation of heat transfer and fluid flow are given in Tables 1 and 2

Table 2 Data used for calculation of temperature and velocity fields

Arc voltage	27 V
Arc current	200, 300, 500 A
Welding velocity	5·2, 12·7, 23·2 mm s^{-1}
Density	7200 kg m^{-3}
Solidus temperature	1745 K
Liquidus temperature	1780 K
Viscosity of liquid	0·024 N s m^{-2}
Thermal conductivity of solid	20·92 W m^{-1} K^{-1}
Thermal conductivity of liquid	334·72 W m^{-1} K^{-1}
Enthalpy of solid at melting point	$1{\cdot}05 \times 10^6$ J kg^{-1}
Enthalpy of liquid at melting point	$1{\cdot}32 \times 10^6$ J kg^{-1}
Diffusion coefficient of oxygen in steel	1×10^{-8} m^2 s^{-1}
Specific heat of solid	703 J kg^{-1} K^{-1}
Specific heat of liquid	808 J kg^{-1} K^{-1}

Table 3 Interaction coefficients in liquid iron at 1873 K

	C	Si	Mn	Cr	Ni	Al	N	Ti	O	H
C	0·14	0·08	−0·012	−0·024	0·012	0·043	0·11	...	−0·34	0·67
Si	0·188	0·11	0·002	−0·0003	0·005	0·058	0·09	...	−0·23	0·64
Mn	−0·07	0	0	...	...	...	−0·091	...	−0·083	−0·31
Cr	−0·12	−0·0043	...	−0·0003	0·0002	...	−0·19	0·059	−0·14	−0·33
Ni	0·042	0·0057	...	−0·0003	0·0009	...	0·028	...	0·01	−0·25
Al	0·091	0·0056	...	...	...	0·045	−0·058	...	−6·3	0·024
N	0·13	0·047	−0·02	−0·047	0·01	−0·028	0	−0·53	0·05	...
Ti	...	...	...	0·055	...	...	−1·8	0·013	−1·8	−1·1
O	−0·45	−0·131	−0·021	−0·04	0·006	−3·9	0·057	−0·6	−0·23	−3·1
H	0·06	0·027	−0·0014	−0·0022	0	0·013	...	0·013	−0·19	0

respectively. Details of the calculations were given in a previous paper.[20]

Thermodynamics and kinetics of inclusion growth and dissolution

A number of assumptions were made to understand the growth and dissolution of oxide inclusions in the weld pool, namely:

(i) the weld pool is compositionally homogeneous
(ii) the nuclei are spherical and each grows without any interaction with other nuclei; collision and coalescence of inclusions are ignored for simplicity
(iii) local equilibrium prevails at the interface between the inclusion and the liquid metal
(iv) the inclusion growth and dissolution rate can be calculated from the flux of oxygen alone.

The free energy change ΔG associated with the reaction $xM + yO = M_xO_y$ at the interface between an oxide inclusion and liquid steel is

$$\Delta G = \Delta G^0 + RT \ln(a_{M_xO_y}/a_M^x a_O^y) \quad \ldots\ldots\ldots (2)$$

where ΔG^0 is the standard free energy for this reaction; R is the gas constant; T is the temperature; a_M, a_O, and $a_{M_xO_y}$ are the activities of dissolved metal, oxygen, and metal oxide respectively; and x and y are the stoichiometric coefficients. Considering the stoichiometry of the reaction, it is possible to write

$$[M] = [M_{orig}] - (xM_M/yM_O)([O_{orig}] - [O]) \quad \ldots (3)$$

where [M] and [O] are the percentage equilibrium concentrations of metal and oxygen at the interface, $[M_{orig}]$ and $[O_{orig}]$ are the original percentage concentrations of metal and oxygen in the bulk, and M_M and M_O are the atomic weights of metal and oxygen. For simplicity, the nucleation rate of inclusions I_v was calculated considering homogeneous nucleation from

$$I_v = A \exp(-\Delta G^*_{hom}/k_B T)$$
$$= A \exp(-16\pi\sigma^3 V_m^2/3k_B T \Delta G^2) \quad \ldots\ldots (4)$$

Table 4 Parameters for calculation of standard free energy for various oxidation reactions: $\Delta G^0 = a + bT$

Oxidation reaction	a, kJ mol^{-1}	b, kJ mol^{-1} K^{-1}
Fe + O = FeO(l)	−138·78	56·51
2Al + 3O = Al_2O_3(s)	−1208·3	390·9
Ti + 2O = TiO_2(s)	−674·90	233·8
2Ti + 3O = Ti_2O_3(s)	−1087·3	356·3
3Ti + 5O = Ti_3O_5(s)	−1754·3	568·5
Si + 2O = SiO_2(s)	−589·17	228·3
Mn + O = MnO(s)	−287·65	125·2
Fe + 2Al + 4O = FeO.Al_2O_3(s)	−1380·2	453·5
Mn + 2Al + 4O = MnO.Al_2O_3(s)	−1543·99	523·42

where ΔG^*_{hom} is the activation energy for the formation of the oxide nucleus for homogeneous nucleation, A is a constant, k_B is Boltzmann's constant, σ is the interfacial energy of the inclusion equal to 0·5 J m^{-2},[18] V_m is the molar volume of the oxide inclusion, and ΔG can be calculated from equation (2). The interaction coefficients[27] and the standard free energies of formation of oxides are given in Tables 3 and 4. The composition of the steel[18] was Fe–0·066C–0·82Si–1·66Mn–0·05Cr–0·03Ni–0·026Al–0·007N–0·025Ti–0·084O (wt-%). For the overall reaction kinetics involving long range diffusion and precipitation, the extent of transformation ζ as a function of time t is given by[18]

$$\zeta = 1 - \exp\{-[(c_M^i - c_M^{ii})/(c_M^l - c_M^{ii})] I_v (8\pi/15)(\alpha_3^*)^3 t^{5/2}\} \quad \ldots\ldots\ldots (5)$$

where c_M^l is the nominal concentration of metal element far away from the inclusion/liquid interface, c_M^i and c_M^{ii} are the concentrations of metal in the inclusion and at the inclusion/liquid interface respectively, and α_3^* is the parabolic thickening rate constant. For a given steel composition, the TTT diagram of various oxide inclusions can be calculated using equations (2)–(5). These equations were used in a previous paper[18] to calculate the TTT diagram for inclusion formation. In the present paper, the calculations were extended by following loci and temperature excursions of a large number of growing inclusions to understand their growth.

The growth and dissolution rates of small spherical inclusions are assumed to be limited by the transport of oxygen in the alloy. Several approximations can be used to solve the diffusion equation.[28–30] These are the invariant field space (Laplace), invariant size (stationary interface), and linear gradient approximations. Aaron *et al.*[28] evaluated the accuracy of these approximations and found that the stationary interface approximation is more accurate than the other assumptions. This group also found that the result obtained assuming Laplace approximation was almost the same as that obtained assuming the stationary interface approximation in many alloy systems during growth. However, the expression obtained assuming the Laplace approximation is considerably simpler

$$r = (-kD_O t)^{1/2} = \alpha_3^* t^{1/2} \quad \ldots\ldots\ldots\ldots (6)$$

where r is the radius of the inclusion, D_O is the diffusion coefficient of oxygen in the alloy, t is the growth time after nucleation, and α_3^* is given by

$$\alpha_3^* = (-D_O k)^{1/2} \quad \ldots\ldots\ldots\ldots\ldots (7)$$

provided that $|k| \ll 1$, for the constant k defined as

$$k = 2(c_O^{ii} - c_O^l)/(c_O^i - c_O^{ii}) \quad \ldots\ldots\ldots\ldots (8)$$

where c_O^l is the nominal concentration of oxygen far away from the inclusion/liquid interface and c_O^i and c_O^{ii} are the concentrations of oxygen in the inclusion and at the inclusion/liquid interface respectively.

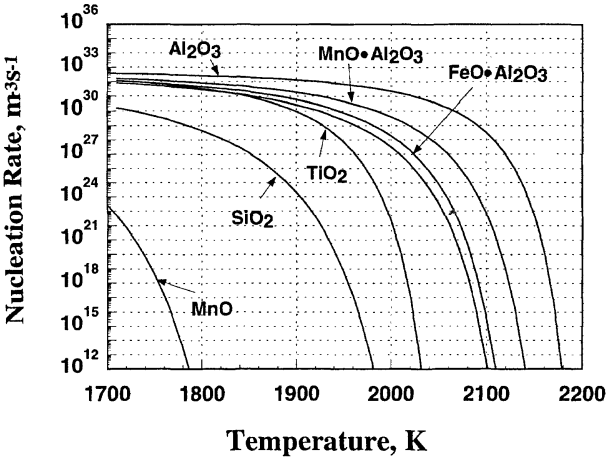

1 Effect of temperature on nucleation rate for various oxide inclusions

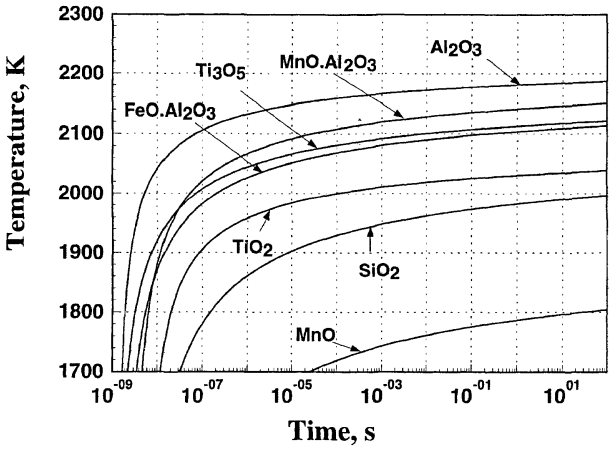

2 Temperature–time–transformation diagram for various oxide inclusions

The velocity of the moving interface between the inclusion and the liquid metal v can be written as

$$v = \mathrm{d}r/\mathrm{d}t = (\mathrm{d}\alpha_3^*/\mathrm{d}t)t^{1/2} + \alpha_3^*/2t^{1/2} \quad (9)$$

The value of c_O^{il} is a function of temperature and alloy composition. As a result, for a given composition, k and α_3^* depend on temperature. The relationship between α_3^* and temperature is calculated from equations (2), (3), (6), and (8). It was found from the calculated results that α_3^* changes by less than 10% when the temperature changes from 1700 to 2200 K, so its change with temperature (and time) may be neglected.

From equation (9), the change in the radius Δr during a small time step Δt can be written as

$$\Delta r = (\alpha_3^*/2t^{1/2})\Delta t \quad (10)$$

The new radius of the inclusion after the time step is given by

$$r_1 = r_0 + \Delta r \quad (11)$$

where r_0 and r_1 are the radii before and after the time step respectively.

For the dissolution of the inclusions, the solution of the diffusion equation with a stationary interface approximation was considered by Whelan.[29] By considering the Laplace approximation for short times, Whelan obtained the simple approximate solution

$$\Delta r = (-k/2)[(D_O/r) + (D_O/\pi t)^{1/2}]\Delta t \quad (12)$$

where D_O is the oxygen diffusion coefficient in the bulk. Because the inclusions move rapidly in the elevated temperature regions, the concentration field near an inclusion is assumed to be constant during the dissolution of oxide. Therefore, the Laplace equation is appropriate for the situation considered here.

Calculation of life cycle of inclusions in weld pool

A calculation procedure was developed to trace trajectories of inclusion particles during their transport within the weld pool. The time steps were calculated in an adaptive way. A submerged inclusion is moved by forces of buoyancy, drag, and inertia. The buoyancy force is small compared with the drag force for usual weld pool conditions and is neglected in the present work. The inertia force acting on the particle is also neglected for simplicity. Therefore, the particles considered here are massless and follow stream lines through the velocity field in the weld pool according to

$$r_1 = r_0 + v \cdot \Delta t \quad (13)$$

$$v = v(r_0) \quad (14)$$

where r_1 is the new location vector, r_0 is the old location vector, v is the velocity value at the old location, and Δt is the adaptive time step. For each time step, the new location and corresponding temperature and velocity values can be obtained.

To understand if inclusion growth is limited by the extent of metal supply during the inclusion's life cycle, the supply and consumption rates of aluminium along the moving path of a specific particle in the weld pool were estimated. The consumption rate R_c is given by

$$R_c \simeq \rho_i(V_1 - V_0)[xM_M/(xM_M + yM_O)]/\Delta t \quad (15)$$

where ρ_i is the density of oxide inclusion and V_1 and V_0 are the volume of inclusion before and after the time step Δt. The supply rate of aluminium in a volume travelled by an inclusion particle R_s is given by

$$R_s = V_p\rho_l[M] = Sv\rho_l[M] \quad (16)$$

where V_p is the volume of the space that the inclusion passes along its path per unit time, S is the cross-sectional area of the inclusion, ρ_l is the density of liquid, and, in this case, [M] is the concentration of aluminium in steel and v is the velocity of the inclusion. The ratio R_c/R_s was found to be about 0·001, so the rate of inclusion formation was not affected by the lack of supply of aluminium.

RESULTS AND DISCUSSION

The nucleation rates of various inclusions calculated from equation (4) are shown in Fig. 1. For the formation of alumina inclusions, the calculated nucleation rates are quite high, up to about 2100 K. The rate decreases with an increase in temperature and becomes very low above 2200 K. Since these rates are calculated from a homogeneous nucleation model, the actual nucleation rate is expected to be somewhat higher. The calculated TTT diagram for a 1% completion of reaction shows that the sequence of inclusion formation is: Al_2O_3, $MnO.Al_2O_3$, Ti_3O_5, $FeO.Al_2O_3$, TiO_2, SiO_2, MnO (Fig. 2). These calculated results show that Al_2O_3 is the most stable oxide inclusion. The curve representing the formation of alumina levels off at about 2200 K, since above this temperature the nucleation rate is very low. Calculation shows that alumina will dissociate at temperatures above about 2240 K for the alloy composition considered in the present work. Furthermore, the rate of supply of alumina in the weld pool from the melting of the baseplate is higher than the rate of oxidation. The calculations show that the consumption rate is about 0·1% of the supply rate. Therefore, for the conditions considered in the present work, the growth of Al_2O_3 inclusions is not limited by the lack of supply of aluminium.

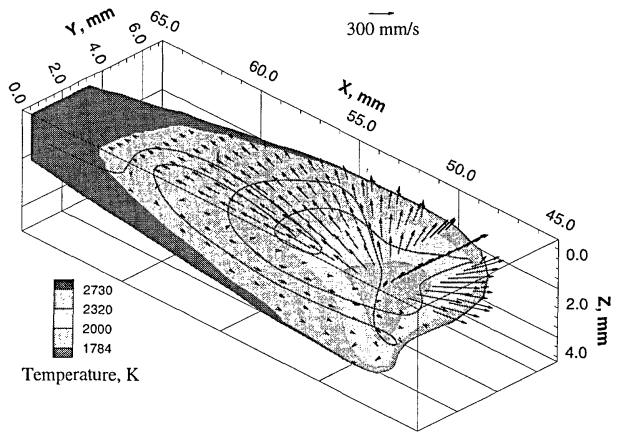

3 Temperature and velocity fields and typical path of particle in weld pool: arc voltage = 27 V, arc current = 300 A, welding velocity = 12·7 mm s^{-1}

The calculated temperature field in Fig. 3 is typical of fusion welding, showing higher temperature gradients ahead of the heat source than behind it. Since the spatial gradient of temperature determines the Marangoni stress, and the Marangoni force is a major driving force for the circulation of liquid metal in the weld pool, the velocities ahead of the weld pool are somewhat higher than those behind the heat source. The velocities in the weld pool are radially outward, i.e. away from the heat source towards the periphery of the weld pool. Temperature is highest near the heat source and decreases away from this region. The resulting Marangoni stress leads to fluid convection in the weld pool. The weld pool shape obtained from the temperature field shows a typical elongated profile and the calculated weld pool depth and width were in good agreement[26] with the corresponding

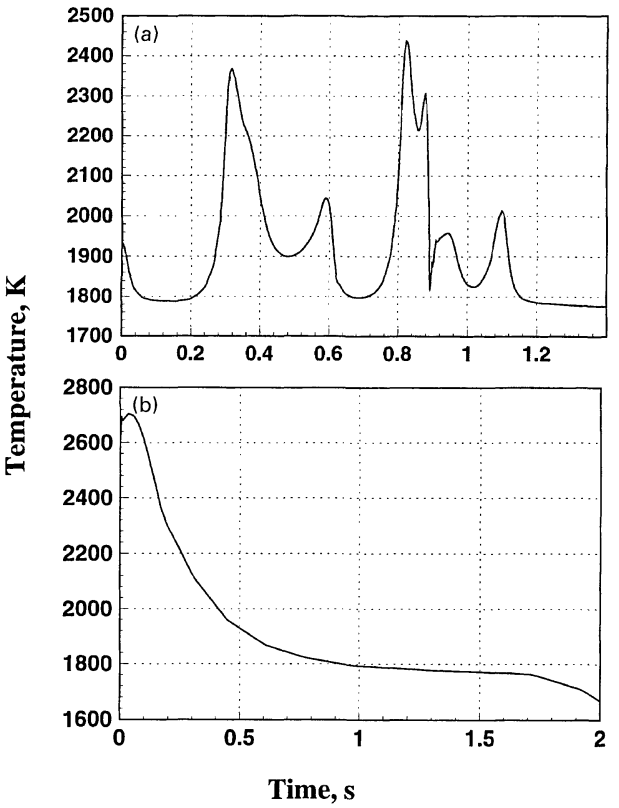

a along path of particle shown in Fig. 3; *b* of particle experiencing continuous cooling behaviour after nucleation

4 Temperature–time plot

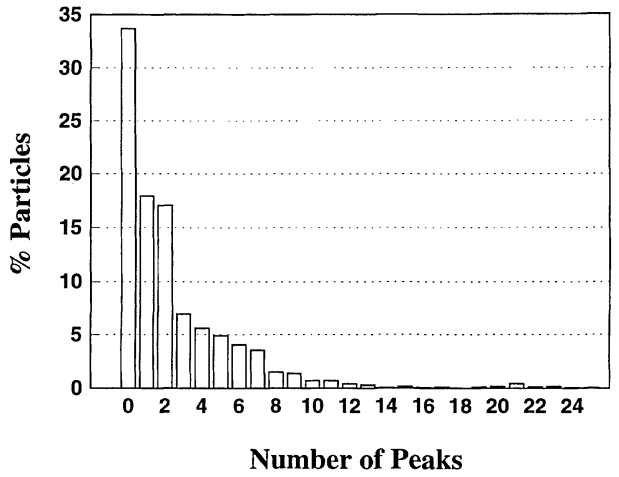

5 Distribution of number of peaks for all particles: arc voltage = 27 V, arc current = 300 A, welding velocity = 12·7 mm s^{-1}

experimental data. This agreement indicates the suitability of the calculation procedure and provides a basis for understanding inclusion growth considering the recirculatory motion in the weld pool and the temperature excursion experiences of the inclusions.

Using the velocity field shown in Fig. 3, the loci of various particles in the weld pool were calculated. Since the inclusions can nucleate in all regions within the weld pool where they are stable, various starting locations for inclusion growth were considered. The number of grid points within the liquid region depended on the welding variables, while the total number of grids was kept constant at 56 × 28 × 28. In the present calculations, at least 1100 grid points were always located within the liquid weld pool. A typical locus of a particle is also shown in Fig. 3. It is observed that the particle undergoes significant recirculatory motion in the weld pool. The corresponding temperature gyrations along the path of the particle are shown in Fig. 4*a*. In most cases, the temperature–time plots of the particles had several characteristic peaks, which characterise the recirculatory nature of the particle paths. However, a large proportion of the inclusions experienced continuous cooling after they were nucleated. Such behaviour is shown in Fig. 4*b*. For the typical welding condition of case 2 listed in Table 1, about 34% of the particles exhibited continuous cooling as shown in Fig. 5. The nature of the temperature–time plot depends on the initial location of the particle. It is also shown in Fig. 5 that some particles experienced more than

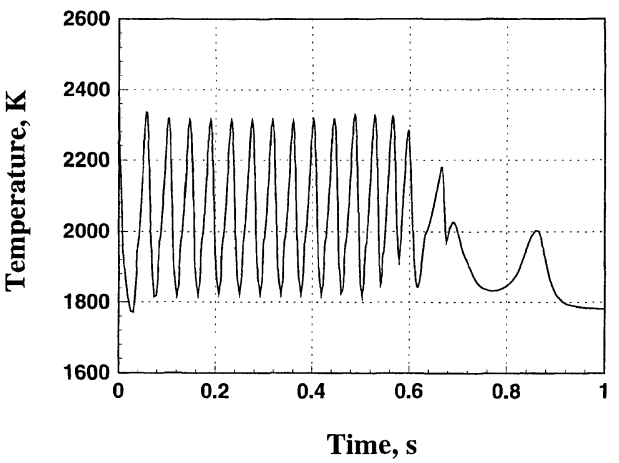

6 Temperature–time plot of particle experiencing more than 20 characteristic peaks

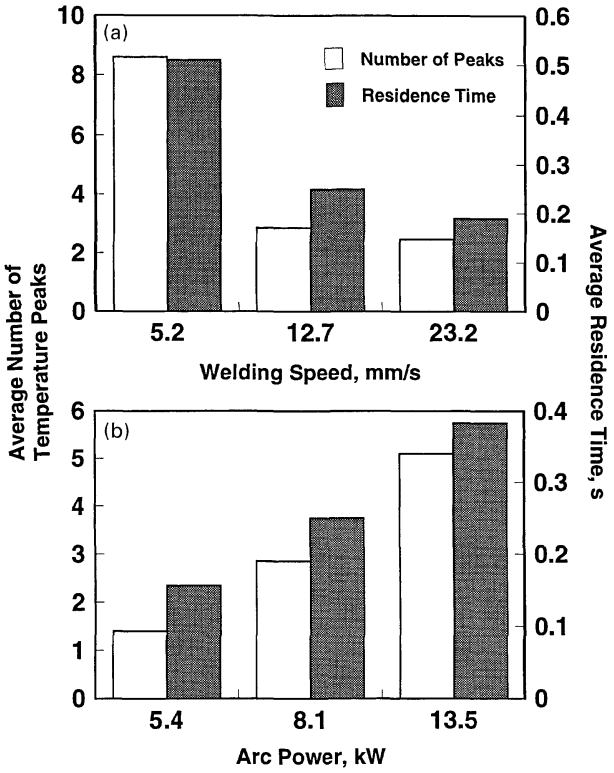

a for constant arc power of 8·1 kW and different welding velocities; *b* for constant welding speed of 12·7 mm s^{-1} and various arc powers

7 Average number of peaks and average residence time

20 temperature peaks. The temperature gyrations experienced by such a particle are shown in Fig. 6. In view of the differences in the temperature gyrations experienced by different particles, it is important to examine the average number of temperature peaks in the life cycle of the inclusions in the weld pool.

The average number of peaks in the temperature–time plots depends on the welding conditions. For example, when arc power is kept at 8·1 kW and welding speed is increased from 5·2 to 23·2 mm s^{-1}, the average number of peaks decreases from 8·6 to 2·4 (Fig. 7*a*). The reduction in the number of peaks is accompanied by the lower residence time of the particles at high welding speeds. The average residence time decreases from 0·53 to 0·18 s (Fig. 7*a*) when

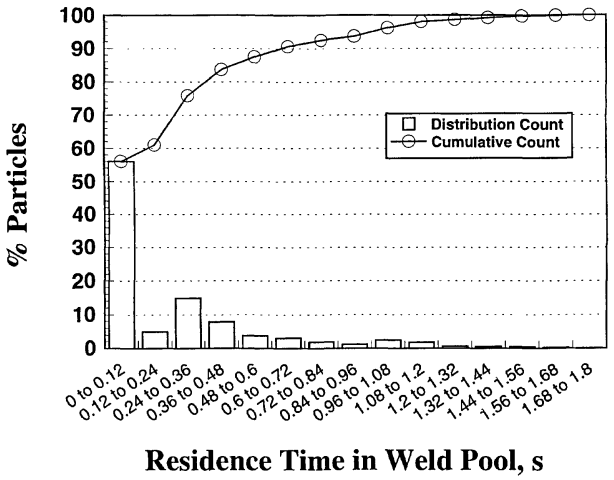

8 Cumulative residence time distribution of all particles: arc voltage = 27 V, arc current = 300 A, welding velocity = 12·7 mm s^{-1}

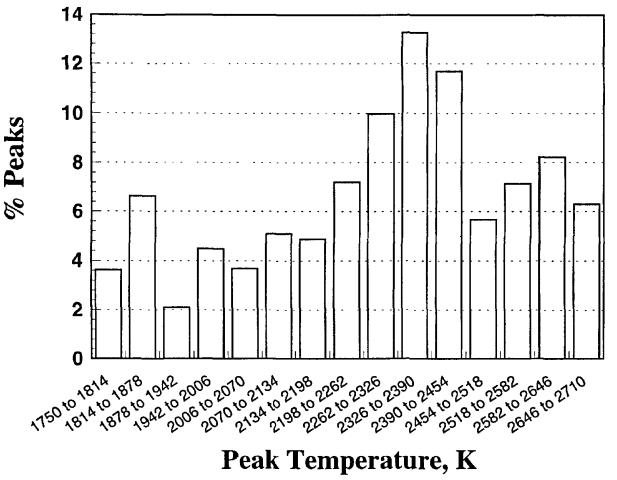

9 Peak temperature distribution of inclusions

the welding speed increases from 5·2 to 23·2 mm s^{-1}. When the welding speed is kept constant at 12·7 mm s^{-1} and the arc power is changed from 5·4 to 13·5 kW, the average number of peaks changes from 1·5 to 5·2 (Fig. 7*b*). Again, the increase is consistent with the increase in the residence time of the particles, as can be observed from the results in Fig. 7*b*, which shows that when arc power changes from 5·4 to 13·5 kW, the average residence time changes from 0·16 to 0·38 s, primarily because of the enlargement of the pool size at higher values of arc power. The residence time of 90% of particles in the weld pool is less than 0·7 s, as shown in Fig. 8. The average residence time is about 0·25 s for the case 2 welding conditions in Table 1.

The highest temperature that the particles can attain has a wide distribution, from the melting point of 1750 K to the highest temperature of about 2710 K, as shown in Fig. 9. It should be noted that when the time average temperatures experienced by the particles are determined by considering temperatures in close proximity of the particles ($=\Sigma T\Delta t/\Sigma\Delta t$, where T is the instantaneous temperature), the resulting temperature (2040 K) is found to be much lower than the mean temperature (2230 K) between the liquidus temperature (1750 K) and the highest temperature (2710 K) in the weld pool. The reason for the lower than average temperature experienced by the inclusions can be understood from consideration of the velocity and the temperature fields in the weld pool. The weld pool temperatures are highest where the heat source impinges on the weld pool surface. The liquid metal velocities are also highest in this region. Because of the high velocities prevail-

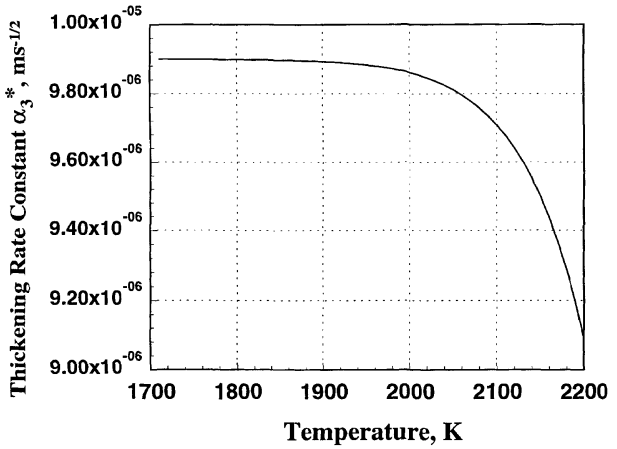

10 Effect of temperature on thickening rate constant of Al_2O_3

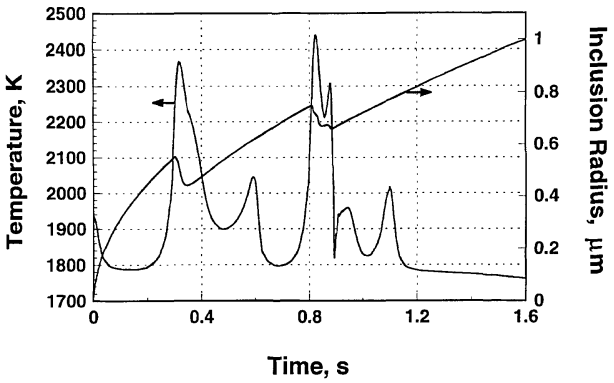

11 Typical inclusion temperature gyration and corresponding size change in weld pool: arc voltage = 27 V, arc current = 300 A, welding velocity = 12·7 mm s^{-1}

ing in the high temperature regions of the pool, the particles spend shorter periods in the hot regions and longer periods in the relatively cold regions. As a result, the time average temperatures are always lower than the average of the liquidus temperature and the peak temperature in the weld pool. An important implication of this finding is that when the isothermal inclusion growth calculations are performed assuming a simple mean weld pool temperature, the calculated inclusion growth rate will be incorrectly predicted. In the case of injection of particles into the molten pool to achieve surface alloying, dissociation of inorganic compounds may also be predicted by such a simple (and inaccurate) assumption, although, in practice, dissociation may not occur because of the low time average temperature actually experienced by the particles.

For the low alloy steel composition given above, the calculated values of α_3^* at various temperatures are shown in Fig. 10. The results show that the rate constant is virtually constant at temperatures lower than about 2000 K. At temperatures above 2200 K, the growth rate decreases. A typical temperature–time plot and the corresponding inclusion radius *v.* time plot are shown in Fig. 11. It can be seen that this inclusion begins to dissolve above about 2240 K and grows again when the temperature falls below 2200 K. The inclusion's radius reaches about 0·95 μm before it is lodged in the solidifying weld metal. From Fig. 9 it can be seen that the majority of the inclusions are exposed to temperatures above 2240 K. Therefore, the effect of dissolution on the inclusion size distribution must be considered. The calculated equilibrium dissolution temperature of Al_2O_3 is about 40 K higher than the maximum temperature for growth observed in the TTT diagram in Fig. 2. This temperature gap results from the very low nucleation rate above 2200 K considered in the model. The enhanced heterogeneous nucleation rate will increase the highest temperature at which alumina can form and, therefore, decrease the 40 K temperature gap. Figure 12*a–c* provides a more complete picture of the inclusion size distributions for three different welding conditions (cases 2, 4, and 5 in Table 1). It can be seen that most inclusions are smaller

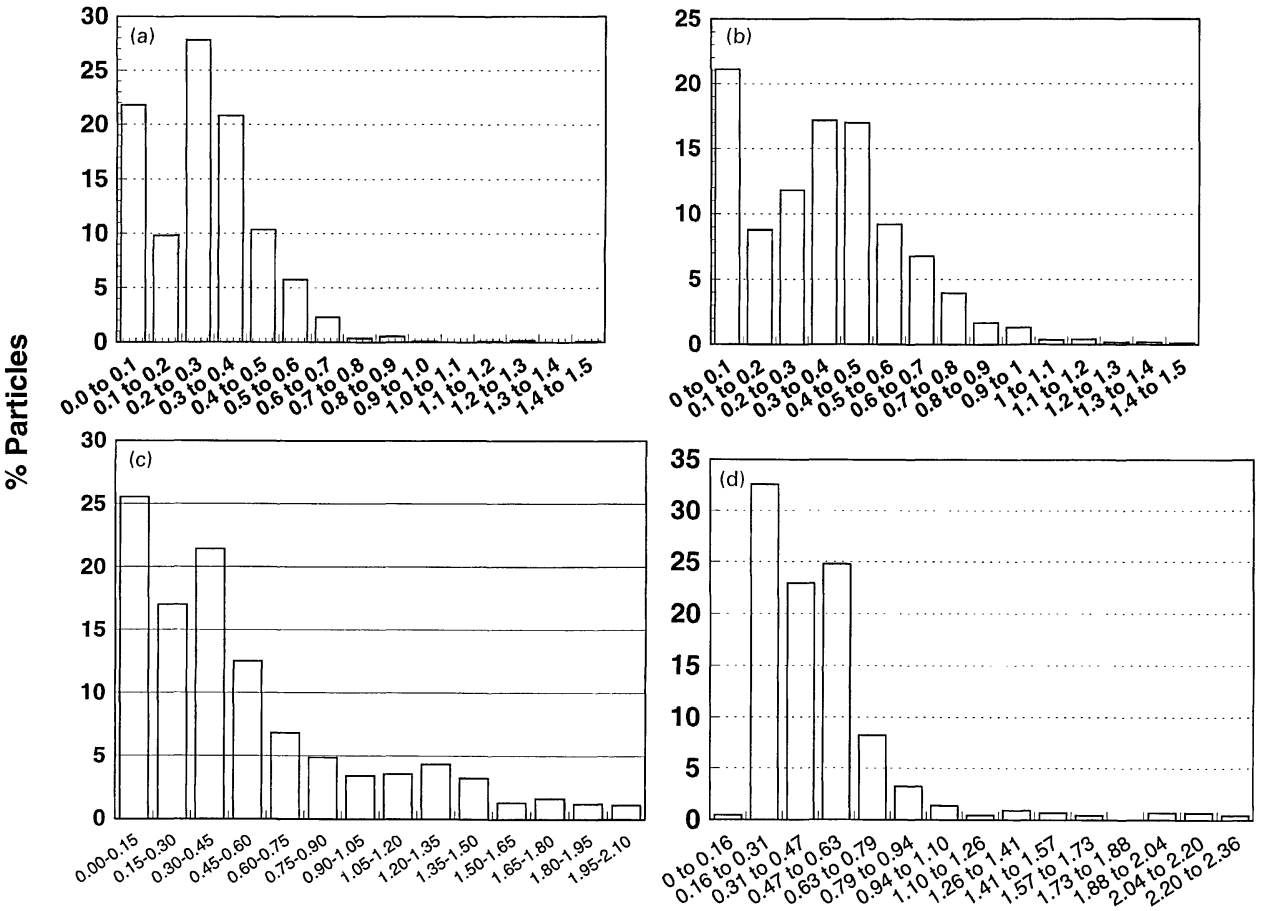

a for arc voltage = 27 V, arc current = 300 A, welding velocity = 23·2 mm s^{-1}; *b* for arc voltage = 27 V, arc current = 300 A, welding velocity = 12·7 mm s^{-1}; *c* for arc voltage = 27 V, arc current = 300 A, welding velocity = 5·2 mm s^{-1}; *d* of experimental results redrawn from Ref. 10

12 Inclusion size distribution

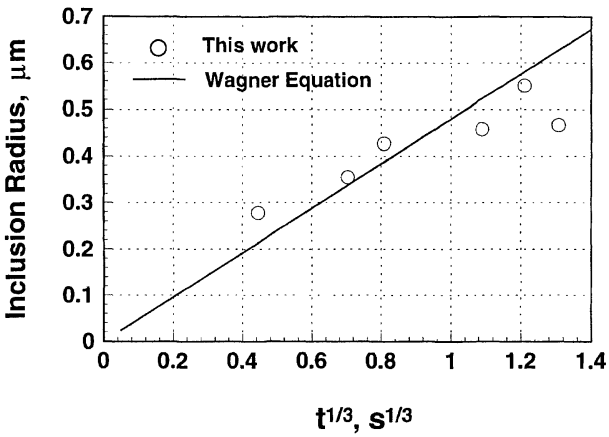

13 Comparison of inclusion sizes calculated from present work and Wagner equation

than 1 μm. Larger inclusion sizes are achieved at low welding velocities. The coarsening of the inclusions is facilitated by the longer times available at low welding speeds. Furthermore, the size distribution curve becomes flatter when the welding velocity decreases. The calculated size distribution is in good agreement with the measured values[19] shown in Fig. 12*d*. Diameters experimentally determined from cross-sections were converted to actual diameters assuming Fullman theory[9,31] for a polydispersed system of spheres. The main difference between the experimental and the calculated results is that the measured values show fewer small particles in the size range of 0–0·16 μm. A possible reason is that small inclusions are difficult to detect in micrographs. However, they are easily accounted for in the calculated result.

In the past, the mechanism of inclusion growth has been investigated by examining how the inclusion radius changes with time. For example, if the inclusions grow by Ostwald ripening[30,32] at the liquidus temperature, and the diffusion of oxygen is considered, the expression of final mean inclusion diameter $\bar{d}$ as a function of t is given by the Wagner equation

$$\bar{d}^3 = \bar{d}_{\text{ini}}^3 + (64\sigma D_O C_O V_m/9RT)t \simeq Ct \quad . \quad . \quad . \quad . \quad . \quad (18)$$

where $\bar{d}_{\text{ini}}$ is the initial mean diameter of inclusions, σ is the oxide–steel interfacial energy, C_O is the bulk oxygen concentration, V_m is the molar volume of the oxide, and C is a proportionality constant. The calculated mean size from the Wagner equation and the sizes of several inclusions as a function of $t^{1/3}$ are shown in Fig. 13. It is interesting to observe that the calculated results show good agreement with the Wagner equation, although the growth and dissolution of the inclusions were calculated assuming diffusion control and non-isothermal temperature gyrations experienced by the inclusions. These results do not rule out the possibility of Ostwald ripening. What they do show is that examining the mechanism of inclusion growth based on how the inclusion size varies with time can lead to completely misleading conclusions.

CONCLUSIONS

1. The growth and dissolution of oxide inclusions in the weld pool were examined considering their recirculatory motion in the weld pool and their temperature gyration experiences. Equations of conservation of mass, momentum, and energy were solved numerically to understand the fluid flow pattern and temperature fields in the weld pool. The recirculatory motion in the weld pool and the temperature history of each of the inclusions were considered to examine their diffusion controlled growth and dissolution.

2. For the welding conditions considered, the weld pool geometry had a typical elongated profile. The computed pool dimensions agreed well with the corresponding measured values.

3. The calculated TTT diagrams showed the sequence of inclusion formation to be: Al_2O_3, $MnO.Al_2O_3$, Ti_3O_5, $FeO.Al_2O_3$, TiO_2, SiO_2, MnO for the given steel composition. The supply rate of aluminium was considerably higher than its oxidation rate.

4. Temperature–time plots for the inclusion particles in many cases displayed several characteristic temperature peaks. However, about one-third of the particles experienced continuous cooling behaviour.

5. The average residence time of the particles in the weld pool and their size distributions were affected by the welding conditions. Calculated results showed that the residence time decreased with higher welding speeds and lower welding powers. The inclusions were coarser at low welding speeds and high welding powers.

6. Good agreement between the calculated and experimentally observed inclusion size distribution indicates that inclusion growth can be understood from the fundamentals of transport phenomena and kinetics.

7. The increase in inclusion size with time exhibited a pattern characteristic of Ostwald ripening, although the growth and dissolution of the inclusions were calculated assuming diffusion control and non-isothermal temperature gyrations experienced by the inclusions.

ACKNOWLEDGEMENTS

The present study was supported by a grant from the US Department of Energy, Office of Basic Energy Sciences, Division of Materials Sciences. The authors would like to thank Dr K. Mundra, Dr S. A. David, Dr R. Ebner, and Dr S. S. Babu for helpful discussions.

REFERENCES

1. S. A. DAVID and T. DEBROY: *Science*, 1992, **257**, 497–502.
2. T. DEBROY and S. A. DAVID: *Rev. Mod. Phys.*, 1995, **67**, (1), 85–112.
3. H. K. D. H. BHADESHIA, L.-E. SVENSSON, and B. GRETOFT: *Acta Metall.*, 1985, **33**, 1271.
4. H. K. D. H. BHADESHIA and L.-E. SVENSSON: in 'Mathematical modelling of weld phenomena', (ed. H. Cerjak and K. E. Easterling), 109–180; 1993, London, The Institute of Materials.
5. H. K. D. H. BHADESHIA: in 'International trends in welding science and technology', (ed. S. A. David and J. M. Vitek), 213; 1993, Materials Park, OH, ASM International.
6. K. MUNDRA, T. DEBROY, S. S. BABU, and S. A. DAVID: *Weld. J. Res. Suppl.*, 1997, **76**, 163–171.
7. Z. YANG and T. DEBROY: *Sci. Technol. Weld. Joining*, 1997, **2**, (2), 53–58.
8. L.-E. SVENSSON, B. GRETOFT, and H. K. D. H. BHADESHIA: *Scand. J. Metall.*, 1986, **15**, 97–103.
9. A. KLUKEN and Ø. GRONG: *Metall. Trans. A*, 1989, **20**, 1335–1349.
10. Ø. GRONG and D. K. MATLOCK: *Int. Met. Rev.*, 1986, **31**, (1), 27–48.
11. Ø. GRONG, T. A. SIEWERT, G. P. MARTINS, and D. L. OLSON: *Metall. Trans. A*, 1986, **17**, 1797–1807.
12. C. S. CHAI and T. W. EAGAR: *Metall. Trans. B*, 1981, **12**, 539–547.
13. C. S. CHAI and T. W. EAGAR: *Weld. J.*, 1982, **61**, 229–232.
14. U. MITRA and T. W. EAGAR: *Metall. Trans. B*, 1991, **22**, 65–71.
15. U. MITRA and T. W. EAGAR: *Metall. Trans. B*, 1991, **22**, 73–81.
16. U. MITRA and T. W. EAGAR: *Metall. Trans. B*, 1991, **22**, 83–100.
17. D. L. OLSON, S. LIU, and G. R. EDWARDS: in 'Mathematical modelling of weld phenomena', (ed. H. Cerjak and K. E. Easterling), 89–108; 1993, London, the Institute of Materials.
18. S. S. BABU, S. A. DAVID, J. M. VITEK, K. MUNDRA, and T. DEBROY: *Mater. Sci. Technol.*, 1995, **11**, (2), 186–199.
19. S. S. BABU, S. A. DAVID, and T. DEBROY: *Sci. Technol. Weld. Joining*, 1996, **1**, (1), 17–27.
20. K. MUNDRA, T. DEBROY, and K. M. KELKAR: *Numer. Heat Transfer A*, 1996, **29**, 115–129.

21. W. PITSCHENEDER, T. DEBROY, K. MUNDRA, and R. EBNER: *Weld. J. Res. Suppl.*, 1996, **75**, 71–80.
22. V. R. VOLLER and C. PRAKASH: *Int. J. Heat Mass Transfer*, 1987, **30**, (12), 2690–2694.
23. A. D. BRENT, V. R. VOLLER, and K. J. REID: *Numer. Heat Transfer*, 1988, **13**, 297–318.
24. S. V. PATANKAR: 'Numerical heat transfer and fluid flow'; 1980, New York, NY, Hemisphere.
25. S. V. PATANKAR: Documentation for COMPACT–3D software, Version 3.1, Innovative Research Inc., Minneapolis, MN, 1994.
26. K. MUNDRA, J. BLACKBURN, and T. DEBROY: *Sci. Technol. Weld. Joining*, 1997, **2**, (4), 174–184.
27. G. K. SIGWORTH and J. F. ELLIOTT: *Met. Sci.*, 1974, **21**, 298–310.
28. H. B. AARON, D. FAINSTEIN, and G. R. KOTLER: *J. Appl. Phys.*, 1970, **41**, 4404–4410.
29. M. J. WHELAN: *Met. Sci. J.*, 1969, **3**, 95–97.
30. Ø. GRONG: 'Metallurgical modelling of welding', 317; 1994, London, The Institute of Materials.
31. R. L. FULLMAN: *Trans. AIME*, 1953, **197**, 447–452.
32. L. RATKE and W. K. THIERINGER: *Acta Metall.*, 1985, **33**, 1793–1802.